nanomaterials

MDPI

Article

One-Step Hydrothermal Synthesis of Cu_2ZnSnS_4 Nanoparticles as an Efficient Visible Light Photocatalyst for the Degradation of Congo Red Azo Dye

Rodrigo Henríquez [1,*], Paula Salazar Nogales [1], Paula Grez Moreno [1], Eduardo Muñoz Cartagena [1], Patricio Leyton Bongiorno [1], Elena Navarrete-Astorga [2] and Enrique A. Dalchiele [3]

[1] Instituto de Química, Facultad de Ciencias, Pontificia Universidad Católica de Valparaíso, Casilla 4059, Valparaíso 2340000, Chile; paula.salazar@pucv.cl (P.S.N.); paula.grez@pucv.cl (P.G.M.); eduardo.munoz.c@pucv.cl (E.M.C.); patricio.leyton@pucv.cl (P.L.B.)
[2] Laboratorio de Materiales y Superficie, Departamento de Física Aplicada I, Universidad de Málaga, 29071 Málaga, Spain; enavarrete@uma.es
[3] Instituto de Física, Facultad de Ingeniería, Herrera y Reissig 565, C.C. 30, Montevideo 11000, Uruguay; dalchiel@fing.edu.uy
* Correspondence: rodrigo.henriquez@pucv.cl; Tel.: +56-32-2274921

Abstract: A hydrothermal method was successfully employed to synthesize kesterite Cu_2ZnSnS_4 (CZTS) nanoparticles. X-ray diffraction (XRD), Raman spectroscopy, X-ray photoelectron spectroscopy (XPS), field-emission scanning electron microscopy (FE-SEM), energy-dispersive X-ray spectroscopy (EDS), transmission electron microscopy (TEM), and optical ultraviolet-visible (UV-vis) spectroscopy were used for characterization of structural, chemical, morphological, and optical properties. XRD results confirmed that a nanocrystalline CZTS phase corresponding to the kesterite structure was formed. Raman analysis confirmed the existence of single pure phase CZTS. XPS results revealed the oxidation states as Cu^+, Zn^{2+}, Sn^{4+}, and S^{2-}. FESEM and TEM micrograph images revealed the presence of nanoparticles with average sizes between 7 nm to 60 nm. The synthesized CZTS nanoparticles bandgap was found to be 1.5 eV which is optimal for solar photocatalytic degradation applications. The properties as a semiconductor material were evaluated through the Mott–Schottky analysis. The photocatalytic activity of CZTS has been investigated through photodegradation of Congo red azo dye solution under solar simulation light irradiation, proving to be an excellent photocatalyst for CR where 90.2% degradation could be achieved in just 60 min. Furthermore, the prepared CZTS was reusable and can be repeatedly used to remove Congo red dye from aqueous solutions.

Keywords: CZTS; hydrothermal; Congo red azo dye; photocatalysis

Citation: Henríquez, R.; Nogales, P.S.; Moreno, P.G.; Cartagena, E.M.; Bongiorno, P.L.; Navarrete-Astorga, E.; Dalchiele, E.A. One-Step Hydrothermal Synthesis of Cu_2ZnSnS_4 Nanoparticles as an Efficient Visible Light Photocatalyst for the Degradation of Congo Red Azo Dye. *Nanomaterials* **2023**, *13*, 1731. https://doi.org/10.3390/nano13111731

Academic Editors: Yan Cheng and Huanqin Zhao

Received: 2 May 2023
Revised: 18 May 2023
Accepted: 18 May 2023
Published: 25 May 2023

1. Introduction

In the search of green semiconducting photovoltaic absorber materials alternative to the conventional ones (i.e., CdTe and $Cu(In,Ga)Se_2$), in recent years the quaternary copper compound having the kesterite structure Cu_2ZnSnS_4 (CZTS) has emerged as a potential candidate to replace them for next generation solar cells [1–7]. In addition to its optical and electronic properties, such as an optimal direct band gap (between 1.4 and 1.6 eV), a high absorption coefficient (~10^4 cm^{-1}) (which allows for effective absorption of the incident photons in absorbers with thicknesses of a few microns), an intrinsic *p*-type conductivity, a thermodynamically stable structure, and a three-dimensional symmetry of carrier transport, it is mainly composed of earth-abundant and nontoxic elements (such as Cu, Zn, and Sn) [1–5]. Through theoretical simulations and device modeling, it was concluded that after optimization of a typical solar cell device, CZTS showed excellent solar-to-electrical conversion performance, with an efficiency of 28.2%, compared to CdTe (20.41%) and $Cu(In,Ga)Se_2$ (21.41%) [8]. CZTS solar cells have reached 12.6% efficiency, which is still far

below the theoretical limit, indicating the efficiency potential of kesterite has not been fully exploited [1,2].

Asides from the early and conventional application of CZTS compound in thin film solar cells [1–5,9], more recently, other ones outside its conventional usage, such as in charge-transfer layers, sensors, thermoelectric devices, and water splitting, have now been reported in the literature [10]. For instance, Yokoyama et al. first demonstrated in 2010 the application of CZTS as a photocathode [10,11]. From this work, CZTS became extensively employed as a photocathode for the production of hydrogen from solar-assisted water splitting [10]. Moreover, it has been proven that CZTS films exhibit excellent photoreactivity and photocatalytic performance [12–14]. In recent years, as a promising solar-driven photocatalyst, the CZTS compound has been recognized and intensively studied due to its excellent performances in air purification, and water remediation of organic pollutants and industrial wastes [12,15–22].

As it is well known, most of the properties of nanomaterials are very much dependent on their size, shape, and dimensionality. Further, it is possible to tune their physical and optical properties by varying the nanocrystal size and various synthesis parameters [13,17]. In this sense, higher photocatalytic activity has been exhibited by CZTS in its nano form rather than in its bulk counterpart [17]. Moreover, it has been reported that CZTS with different morphologies has different adsorption and degradation rates of organic pollutants [23].

To produce CZTSs with respectable photocatalytic and photoelectrochemical capabilities, several techniques have been established to date [5]. Several vacuum and non-vacuum thin film deposition techniques, as well as the direct production of kesterite nanocrystals, have been extensively researched among these approaches [5]. In fact, several fabrication techniques have been developed as effective CZTS nanocrystal synthesis methods, such as hot injection, hydrothermal/solvothermal, and microwave-assisted chemical synthesis [5]. Among various wet-chemical processes, hydrothermal/solvothermal CZTS nanocrystal synthesis is a widely favored approach for the controlled production of kesterite nanocrystals [5,24,25]. Moreover, this process is not limited by the temperature and pressure of the vessel, and the reaction does not require the nitrogen atmosphere and refluxing, which on the other hand are highly important parameters for the hot-injection synthetic route [26].

On the other hand, Congo red (CR) is a synthetic azo-anionic dye that has applications in the textile industry and tests for medical diagnosis. However, CR is a known human carcinogen that can also bring various harmful effects to human health [27–30]. Due to this, several works have been developed to study its elimination from aqueous effluents [31–33].

In the present work, Cu_2ZnSnS_4 nanoparticles have been synthesized by the hydrothermal technique. Further, structural, morphological, surface chemical study, optical and optoelectronic characterization of these nanostructures has been carried out. The synthesized sample has been used as a photocatalyst to degrade Congo red azo dye to evaluate the photocatalytic performance of CZTS. Moreover, to our knowledge, it is the first time that the kesterite semiconductor has been investigated and employed as a photocatalyst in the photodegradation of the hazardous Congo red azo dye. Hence, emphasizing the novelty of the current work.

2. Materials and Methods

2.1. Hydrothermal Synthesis

The synthesis of CZTS nanoparticles was performed using a mixture of 2 mmol $CuCl_2$ (Winkler, Langley, BC, Canada), 1 mmol $ZnCl_2$ (Sigma-Aldrich, Oakville, ON, Canada), 1 mmol $SnCl_2$ (Winkler P.A.), and 4 mmol CH_4N_2S (Merck, Rahway, NJ, USA) in a Teflon-coated stainless-steel reactor at 200 °C for 72 h. The pH value of the mother solution was measured employing a pH-meter (BANTE model PHS-25CW) with a value of 6.88 pH unities. The obtained nanoparticles were washed with 1:1 ethanol/water and centrifuged for 15 min at 4500 rpm (DLAB model DM0412). Finally, the CZTS nanoparticles were dried for 6 h at 60 °C in an oven in air atmosphere.

2.2. Characterization of CZTS Nanoparticles

The structural characterization of the CZTS phase was performed by X-ray diffraction (XRD) using a Bruker D8 ADVANCE diffractometer. The operating conditions were: CuKα radiation (30 mA, 40 kV, λ = 0.15418 nm), in Bragg–Brentano 45° mode, with a step of 0.01° and a step time of 34 s at room temperature.

Raman spectra were obtained using a Witec Alpha 300 confocal Raman microscope system equipped using an excitation laser wavelength of 785 nm and an electrically cooled CCD camera. The signal was calibrated using the 520 cm^{-1} line of a Si wafer and a 20× objective. The laser power on the samples was 2 mW. The resolution was set to 4 cm^{-1} and 10 scans with an integration time of 1 s were performed.

The chemical composition of the Cu_2ZnSnS_4 samples was studied via X-ray photoelectron spectroscopy (XPS) using a Physical Electronics (PHI) VersaProbe II spectrometer equipped with an Al Kα radiation source (1486.6 eV and 47.8 W).

Field emission scanning electron microscopy (FE-SEM) images of the CZTS samples were obtained on Helios Nanolab 650 Dual Beam equipment from FEI Company. For this, the powders were supported on conductive carbon tape inside the vacuum chamber. The analysis of the chemical composition of the formed structures was carried out using X-ray energy dispersion spectrometry (EDS). The equipment used was a QUANTAX 200 model from Bruker with XFLASH (EDS coupled to SEM equipment: Hitachi SEM SU-3500 of variable pressure with a detector 410-M). Samples for TEM were ultrasonically dispersed in 1 mL of ethanol. A small drop of the suspended solution was placed on a porous carbon film on a nickel screen and allowed to air dry. Transmission electron microscopy (TEM) and high-resolution transmission electron microscopy (HRTEM) images were obtained on a Talos F200X instrument. To obtain the mean sizes of the kesterite nanoparticles the ImageJ ver. 1.53t software has been used.

Optoelectronic properties of the nanoparticulate Cu_2ZnSnS_4 samples, i.e., optical and semiconducting properties have been verified through optical UV-visible absorption spectrometry measurements and by Mott–Schottky analysis, respectively, as is detailed below.

The optical properties were studied by UV-VIS molecular absorption spectra through the transmittance spectrum, using a SHIMADZU UV-2600 Spectrophotometer with a PC connection. The measurement range was from 400 nm to 900 nm at room temperature, with a scanning speed of 0.2 nm s^{-1}, and 10 mg of CZTS nanoparticles suspended in ethanol were prepared.

Prior to the electrochemical analysis, thin films of CZTS were made using the drop-casting method, with a solution of the compound in ethanol to be placed in FTO (1.5 × 1 cm^2). The films were dried for 4 h at 60 °C in an Ar atmosphere.

To electrochemically characterize the nanoparticles, cyclic voltammetry, and EIS were performed through the Mott–Schottky representation. The conventional cell with three electrodes was used: FTO/CZTS as the working electrode, Ag/AgCl (3M KCl) as the reference electrode, and a platinum wire as the auxiliary electrode, all immersed in a 0.1 M Na_2SO_4 solution as the supporting electrolyte. An AUTOLAB model PGSTAT 302 potentiostat/galvanostat and an FRA ZAHNER model ZENNIUM PP211 potentiostat/galvanostat were used for the measurements. The measurements were developed at room temperature. Mott–Schottky measurements were performed by applying an AC voltage with 10 mV amplitude with a frequency of 10 kHz at open circuit potential (0.03 V vs. Ag/AgCl 3 M), and analyzes were performed in a parallel circuit. In all cases, the area exposed to the supporting electrolyte was 1 cm^2.

2.3. Photodegradation of Congo Red Azo Dye (CR)

For photodegradation, a 50 mL solution of 0.04 mM Congo red azo dye was prepared, to which 35 mg of CZTS nanoparticles were added. The solution was shaken in the dark for 30 min to generate adsorption–desorption equilibrium. Then, the solution was exposed to an ABET Technologies Model 11002 SunLite solar simulator (1000 W), and photodegra-

dation was examined by monitoring the absorption spectra of Congo red azo dye solutions after various irradiation times using a Shimadzu UV-2600 UV-Vis spectrophotometer. The measurement wavelength range was 400–700 nm at room temperature, with a scanning speed of 0.2 nm s^{-1}. Prior to photodegradation, a calibration curve of the CR dye was made, and the following equation was used to determine the *degradation efficiency*:

$$Degradation\ efficiency(\%) = \frac{C_0 - C_t}{C_0} \times 100 \quad (1)$$

where C_0 corresponds to the initial concentration of Congo red azo dye prior to exposure to illumination and C_t corresponds to the concentration of Congo red dye after being exposed to solar illumination for a certain time t.

2.4. Photocatalyst Regeneration Study

The cyclability of the CZTS photocatalyst has been evaluated maintaining the experimental parameters described above. After each cycle, the nanocomposite was collected and washed with ethanol multiple times, dried for 30 min at 60 °C, and then reused for subsequent runs. Naturally, the loss of a portion of the photocatalyst has been observed, and then the amount of CZTS photocatalyst used in each cycle was not maintained.

3. Results

3.1. Structural, Morphological, and Surface Chemical Study

In order to determine structural and morphological properties, and also chemical surface composition, the prepared CZTS samples have been characterized by X-ray diffraction (XRD), Raman spectroscopy, X-ray photoelectron spectroscopy (XPS), field emission-scanning electron microscopy (FE-SEM) and high-resolution transmission electron microscopy (HR-TEM).

Figure 1a shows a typical diffraction pattern of a hydrothermally grown nanoparticulate Cu_2ZnSnS_4 sample. For comparison, the XRD pattern of the standard tetragonal crystalline structure of Cu_2ZnSnS_4 (kesterite), JCPDS pattern #04-023-6315, is also provided. The XRD pattern exhibits four main intense diffraction peaks at 2 θ = 28.6°, 2 θ = 32.9°, 2 θ = 47.6° and 2 θ = 56.3° ascribed to the (112), (200), (220)/(204) and (132)/(116) diffraction planes of the tetragonal crystalline structure of CTZS, respectively. In addition, four other faint diffraction peaks can be seen, which can also be ascribed to the kesterite CZTS phase. Results agree with other XRD structural studies of the kesterite phase previously reported in the literature [12,15,25,34]. Then, the XRD results indicate that the formed kesterite CZTS phase is well-defined, and the samples are polycrystalline. The presence of a very small impurity diffraction peak corresponding to SnO_2 can be appreciated in the 2 θ range from 25° to 35° (see Figure 1a), indicating the presence of a minor SnO_2 impurity secondary phase. Moreover, the broadening of the CZTS diffraction peaks demonstrates the nanocrystalline character of these samples. The average crystallite size was calculated from the full width at half maximum (FWHM) of XRD peaks by using the Scherrer formula [35,36]:

$$D = \frac{k\lambda}{\beta cos\theta} \quad (2)$$

where D is the crystallite diameter, λ is the wavelength of the incident radiation, k = 0.89 is the shape factor, θ is the Bragg angle, and β is the full width at half maximum (FHWM) in radians. The average crystallite size evaluated from the (112) CZTS diffraction peak was ~18 nm, hinting at its nanocrystalline character.

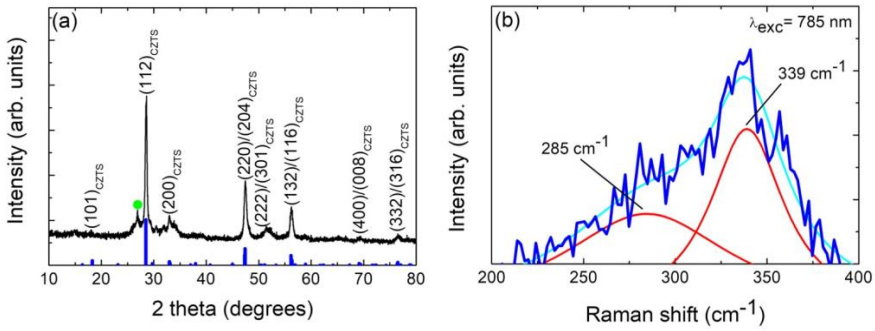

Figure 1. (**a**) X-ray diffraction pattern of a typical nanoparticulate Cu_2ZnSnS_4 sample. Diffraction planes are indicated for the Cu_2ZnSnS_4 phase (CZTS(hkl)). The signal marked with a green symbol (•) corresponds to the cassiterite SnO_2 phase. The tetragonal kesterite JCPDS pattern (#04-023-6315) is also shown for comparison (Cu_2ZnSnS_4 JCPDS: thick blue bars). (**b**) Raman spectrum of nanoparticulate Cu_2ZnSnS_4 nanopowder sample measured with an excitation wavelength of 785 nm, indicating the characteristic peaks. The cyan line is the fit line while the red lines represent each component. The original spectrum is represented by a blue line.

Due to the similar structure of kesterite CZTS and some secondary phases like cubic ZnS and tetragonal Cu_2SnS_3, the CZTS main X-ray diffraction peak is easy to overlap with that of ZnS and Cu_2SnS_3 one [37–40]. Then, Raman scattering spectroscopy is generally adopted to find the co-existing secondary phases which cannot be identified effectively by X-ray diffraction [37–40]. To differentiate various phases, the first-order Raman spectra in the 200–400 cm^{-1} wavenumber region (see Figure 1b) has been analyzed by deconvolution using the Lorentzian peak fitting procedure. Figure 1b shows the presence of a main peak located at 339 cm^{-1} and a secondary one located at 285 cm^{-1} which corresponds to A_1 and A vibrational modes of kesterite CZTS, respectively [38,40–43]. Thus, the results depicted in Figure 1b can allow us to highlight on one hand that the presence of these features are the characteristic peaks of CZTS and close to the reported values. On the other hand, no other peaks corresponding to ZnS (vibrational modes at 275 and 350 cm^{-1}), cubic Cu_2SnS_3 (267, 303, and 356 cm^{-1}), tetragonal Cu_2SnS_3 (297, 337, and 352 cm^{-1}), Cu_2S (267), SnS (189, 219, and 312 cm^{-1}) and SnS_2 (215 and 312 cm^{-1}) are observed [37,40,44], which indicates that the synthesized CZTS presents a good quality with single phase.

The synthesized nanoparticulate Cu_2ZnSnS_4 samples have been analyzed using XPS to check both the presence of Cu, Zn, Sn, and S and to verify the valence states of these constituent elements. The full XPS spectrum of the sample in Figure 2 shows the peaks of Cu, Zn, Sn, and S together with the C, N, and O peaks. It should be noted that the impurity peaks of C and O may be related to the reference or environmental contamination, and N to vestiges of the CH_4N_2S precursor. The valence state of elements in the CZTS was evaluated by high-resolution XPS spectra. Figure 3 shows the XPS high-resolution spectra. High-resolution spectra for all the core levels of interest (Cu 2p, Zn $2p^{3/2}$, Sn $3d^{5/2}$, and S 2p) were acquired, and also Cu LMM Auger transitions for better identification of the charge state for Cu, along with O 1s and C 1s. The spectra were calibrated at C 1s 284.8 eV. According to the Cu 2p spectra, a main peak is shown at 931.6 eV, and a secondary one at 932.1 eV, which can be related to Cu^+ [45], probably due to the CuCl initial solution. As no satellites are visible at the spectra, no Cu^{2+} remains at the surface [4]. The assignment is also consistent with the calculated modified Auger parameter for each component reported to the Cu LMM Auger transition, taking values of 1849.3 and 1849.8 eV, respectively. According to the Zn 2p spectra, the main peak at 1021.5 eV corresponds to Zn^{2+}. In reference to Sn 3d peaks, the mean peak appears at 486.7 eV, being related to SnO_2 [45], possibly formed for the exposure of the samples to the air ambient oxygen. Finally, the S 2p peak was deconvoluted into two peaks: the main peak at 161.3 eV (S $2p_{3/2}$) is related to CuS [46], and the other at 162.5 eV (S $2p_{1/2}$) could be related to rests of the CH_4N_2S compound used for the prepared material.

The valence states of Cu^{+}, Zn^{2+}, Sn^{4+}, and S^{2-} confirm that the synthesized CZTS simple is well consistent with its stoichiometric formula of Cu_2ZnSnS_4 [14].

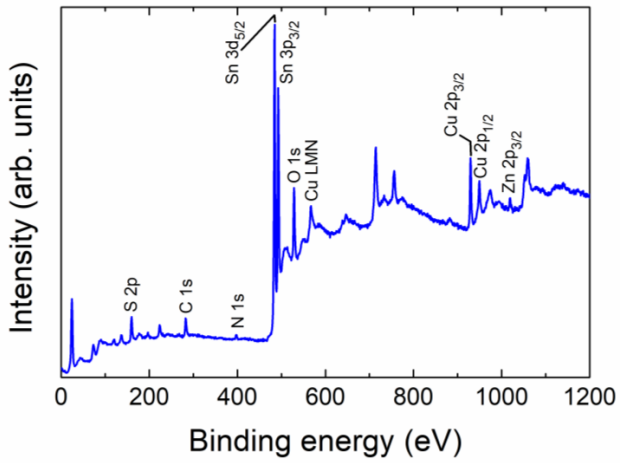

Figure 2. XPS survey spectrum for the synthesized particulate Cu_2ZnSnS_4 sample.

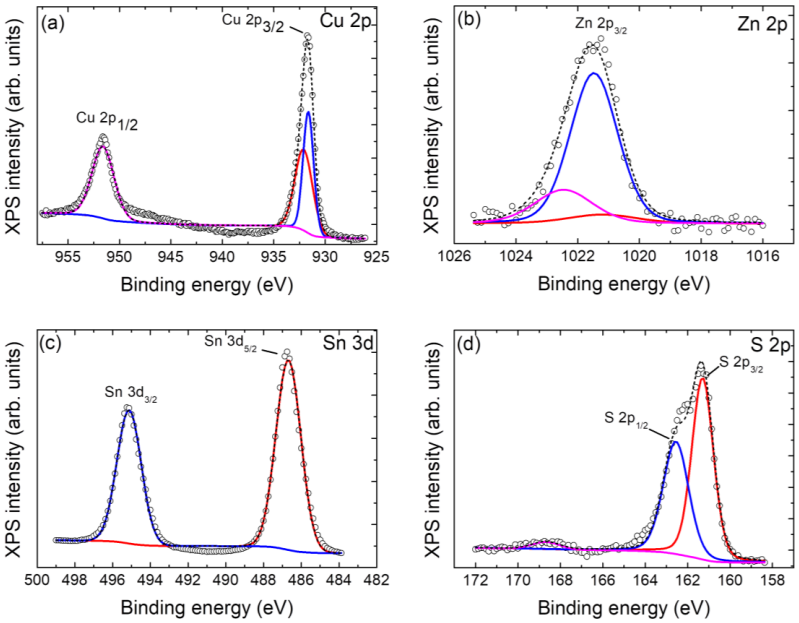

Figure 3. X-ray photoelectron spectroscopy high-resolution spectra for (**a**) Cu 2p, (**b**) Zn 2p, (**c**) Sn 3d, and (**d**) S 2p, for the Cu_2ZnSnS_4 sample. The short dashed black lines are the fit lines while the colored lines represent each component. The original spectra are represented as unfilled dots.

The morphological and microstructural features (i.e., detailed microstructure, size, and shape morphologies), and the chemical composition of the Cu_2ZnSnS_4 samples have been further investigated by field-emission scanning electron microscopy (FE-SEM) and transmission electron microscopy (TEM).

Figure 4a shows a low-magnification FE-SEM micrograph image of a typical hydrothermally synthesized Cu_2ZnSnS_4 sample showing the grain growth structure, revealing the loosely agglomerated CZTS nanoparticles with sizes comprised between 400 to 1200 nm (except for zones where bigger clusters of several microns can be appreciated). Figure 4b shows a higher magnification FE-SEM plan-view micrograph image of a Cu_2ZnSnS_4 sample. It can be seen that the prepared sample exhibits an aggregated morphology of clusters of particles, composed by the congregation of several smaller particles with sizes of about 140 to 200 nm. Moreover, to confirm the presence of all four elements in the nanopowder

sample, the EDS elemental mapping has been conducted and it is shown in the four panels in the lower part of Figure 4a, revealing the presence of Cu, Zn, Sn, and S elements homogeneously distributed in the whole CZTS nanopowder sample. Figure 4c shows a TEM micrograph image of a typical nanoparticulate Cu_2ZnSnS_4 sample, where it can be appreciated the presence of CZTS nanocrystals in the form of spherical and rod-like shapes, as indicated. Similar CZTS nanoparticle shapes have been observed and reported in the literature for CZTS nanocrystals synthesized through a thermolysis route [47]. Figure 4d shows a higher magnification TEM micrograph of the zone highlighted by a dashed yellow circle in Figure 4c, depicting with more detail the presence of spherical CZTS nanocrystals, with an average size of 7 nm (size evaluation considering 100 nanoparticles that can be observed in the micrograph image). Figure 4e,f shows higher magnification TEM micrographs of the rod-like CZTS nanocrystals (see the zone highlighted by a dashed red circle in Figure 4c), exhibiting average diameter sizes in the range of 50 to 60 nm. According to XRD, the mean crystallite size of the CZTS sample is around 18 nm, giving then a mean value of the observed crystallite sizes obtained from the TEM micrographs. However, the obtained values from TEM images are more legitimate [18].

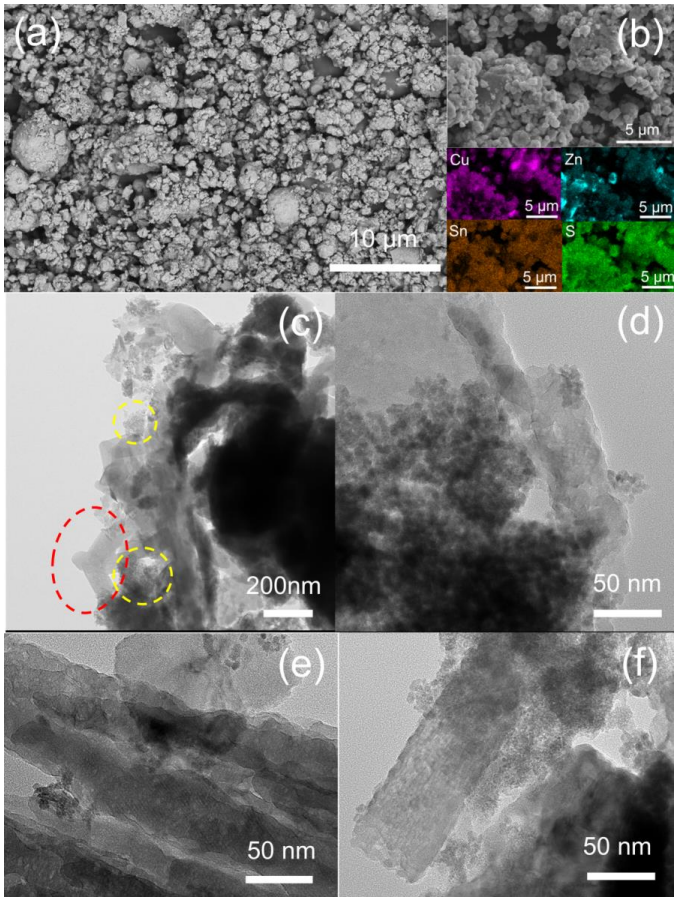

Figure 4. (**a**,**b**) FE-SEM plane-view micrograph images of a typical hydrothermally synthesized nanoparticulate Cu_2ZnSnS_4 sample at two different magnifications and different observed sample areas. EDX elemental mapping of Cu (violet), Zn (cyan), Sn (brown), and S (green) corresponding to Figure 4b FE-SEM micrograph image is depicted in four panels in the lower part of this (**b**). (**c**) Low-magnification TEM micrograph image of a typical hydrothermally synthesized nanoparticulate Cu_2ZnSnS_4 sample. Different CZTS nanocrystal shapes can be visualized: rod-like (indicated by a dashed red circle) and spherical forms (indicated by a dashed yellow circle). (**d**) High-magnification TEM micrograph of one of the zones highlighted by a dashed yellow circle in (**c**). (**e**,**f**) High-magnification TEM micrographs and different observed sample areas of the zone are highlighted by a dashed red circle in (**c**).

3.2. Optoelectronic Characterization

Optoelectronic properties of the nanoparticulate Cu_2ZnSnS_4 samples, i.e., optical and semiconducting properties have been verified through optical UV-visible absorption spectrometry measurements and by Mott–Schottky analysis, respectively.

Figure 5a shows the optical absorption spectrum of a typical nanoparticulate Cu_2ZnSnS_4 sample. From 400 to 700 nm, a moderate decreases of the optical absorption can be appreciated, whereas from 700 to 900 nm optical absorption decreases significantly. The optical bandgap (E_g) and optical transition type of nanoparticulate Cu_2ZnSnS_4 samples have been determined from the Stern relation of near-edge absorption which is given as [36,48–50]:

$$\alpha = \frac{A_0(h\nu - E_g)^n}{h\nu} \quad (3)$$

where A_0 is a parameter related to the effective masses associated with the valence and conduction bands, and $h\nu$ is the photon energy (where ν is the frequency, h is the Planck's constant). m depends on the nature of band transitions, i.e., n = 1/2 or 2 for direct or indirect allowed transitions, respectively. The inset in Figure 5a shows the Tauc plot graph of $(\alpha h\nu)^2$ against hν so the optical bandgap can be determined. For all nanoparticulate Cu_2ZnSnS_4 samples, the optical absorption in the edge region can be well-fitted by this relation, demonstrating that the absorption edge is due to a direct allowed transition, which is in agreement with similar results that have been reported in the literature [12,51–54]. A direct energy optical bandgap of ca. 1.5 eV has been extracted by extrapolating the dashed line in the inset of Figure 5a to the energy axis. This value agrees very well with previous literature-reported values of 1.4 to 1.6 eV [12,26,51–54].

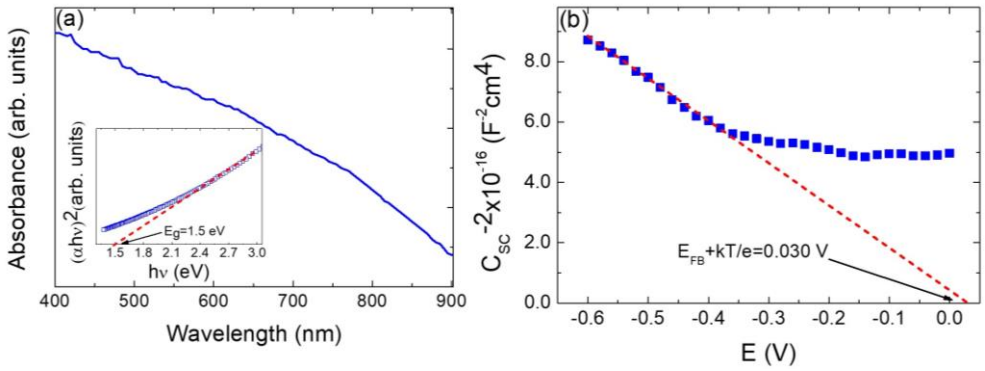

Figure 5. (**a**) UV-visible optical absorbance spectrum of a typical particulate Cu_2ZnSnS_4 sample. Inset: $(\alpha h\nu)^2$ vs. hν Tauc plot, for kesterite bandgap gap energy (E_g) determination and corresponding linear fitting (red dashed line). (**b**) Mott–Schottky plot for a synthesized particulate Cu_2ZnSnS_4 sample. Red dashed line represents the fitted data in the linear range of the curve. The intercept of this line with the x-axis determinates the flat-band potential (E_{FB}) as indicated. Measurements were carried out in 0.1 M Na_2SO_4 (pH = 6.5), with an AC frequency of 10 kHz.

Mott–Schottky (M-S) analysis has been extensively incorporated by the field to assess the main operational parameters of semiconductor photoelectrodes, i.e., the flat-band potential, E_{FB}, and the donor concentration, N_D or acceptor concentration, N_A (for an n-type semiconductor photoanode or a p-type photocathode) [55–57]. The Mott–Schottky equation simply relates the capacitance of the space-charge region (C_{SC}) to the applied potential (E) relative to its E_{FB} and other parameters of the semiconductor as follows [49,55–58]:

$$\frac{1}{C_{SC}^2} = \frac{2}{\varepsilon\varepsilon_0 e N_{D,A}}\left(E - E_{FB} - \frac{k_B T}{e}\right) \quad (4)$$

where ε and ε_0 are the dielectric constant and the vacuum permittivity, respectively, e is the electronic charge, k_B is the Boltzmann constant, and T is the absolute temperature. Accordingly, a plot of ${C_{SC}}^{-2}$ vs. E should reveal E_{FB} as the linearly extrapolated intercept

with the abscissa, while $N_{D,A}$ will be proportional to the inverse of the slope. Figure 5b shows the plot of the inverse of the square of the serial capacitance as a function of the electrochemical potential for a nanoparticulate Cu_2ZnSnS_4 sample electrode. According to the Mott–Schottky equation (Equation (4)), a linear relationship with a negative slope is obtained, confirming that the nanoparticulate Cu_2ZnSnS_4 samples exhibit the semiconductor characteristic of a *p*-type material. A flat band potential value of 0.004 V (considering k_BT/e = 0.026 V at 25 °C) and an acceptor carrier concentration $N_A = 1.5 \times 10^{14}$ cm^{-3} have been obtained.

Thus, this Cu_2ZnSnS_4 *p*-type semiconductor has an extensive range of usages as a photocatalyst because according to the Shockley–Queisser limit, materials have the most visible light absorption of solar light irradiation in this bandgap region, so this bandgap makes it highly activated [59–62]. In fact, the photocatalysts having a bandgap value of around 1.5 eV shows the best photocatalytic efficiency [59–62].

3.3. Photocatalytic Activity Evaluation

The photocatalytic performance of nanoparticulate Cu_2ZnSnS_4 samples has been evaluated by the photodegradation of Congo red azo dye in an aqueous solution under AM1.5G simulated sunlight (100 mW cm^{-2}) illumination. Figure 6a shows the absorption spectra of this dye-aqueous solution, recorded in the wavelength range from 400 to 700 nm. As can be seen (see Figure 6a), the time-dependent absorbance spectra of photodegradation of Congo red dye aqueous solution show a characteristic peak at 497 nm, due to characteristic absorption to be assigned to the n-π^* transition of the lone pair present on the N atom of the azo chromophore (–N=N–) [63]. The absorption peak of the dye diminished with illumination time (indicating that the concentration of Congo red dye decreases), indicating that a photodegradation takes place. Figure 6b shows the relative concentration (C/C_0) changes of CR dye versus the solar simulator irradiation time. To validate the role of synthesized nanoparticulate Cu_2ZnSnS_4 photocatalyst, controlled experiments have also been carried out in the absence of photocatalyst; no significant degradation of CR has been observed (see Figure 6b, red line-symbols). Figure 6b shows that the photocatalytic activity of nanoparticulate Cu_2ZnSnS_4 after one-hour illumination, reaches a 90.2% degradation efficiency value. This value is significantly superior to that attained by TiO_2 Degussa P25 which after one-hour illumination exhibits only a CR degradation efficiency of 70% [64–66]. This can be explained by taking into account that as CZTS is a narrow bandgap semiconductor (E_g = 1.5 eV), under visible light illumination, it has the ability to degrade organic compounds in less time compared to TiO_2 which presents a wide bandgap (E_g = 3.2 eV) [12,18]. Moreover, it must be pointed out that crystallite size worth plays a significant role in improving the photocatalytic performance of photocatalysts. The surface area to volume proportion increases as the crystallite size value decreases, enhancing both the surface-active sites and the interfacial charge carrier transport rate. In the present case, the improved photocatalytic activity of the nanoparticulate Cu_2ZnSnS_4 photocatalyst could also then be attributed to its lowered crystallite size worth.

Furthermore, the observed degradation efficiency is higher than that obtained for the photodegradation of another azo dye such as Rhodamine B, where 83% or 51.7% could be obtained after 100 and 240 min, respectively [13,67]; the fact that may be related to the number of active sites for the generation of radical species given the nanocrystalline nature of our Cu_2ZnSnS_4 phase.

The CR photodegradation has been fitted to a pseudo-first-order kinetic model that can be expressed as follows:

$$ln\frac{C_0}{C} = kt \quad (5)$$

where k is the kinetic rate constant, C_0 is the initial concentration, and C is the concentration at given time t. A constant k of 0.01 min^{-1} was obtained, being comparable to that exhibited by Degussa P25 TiO_2 [68–70].

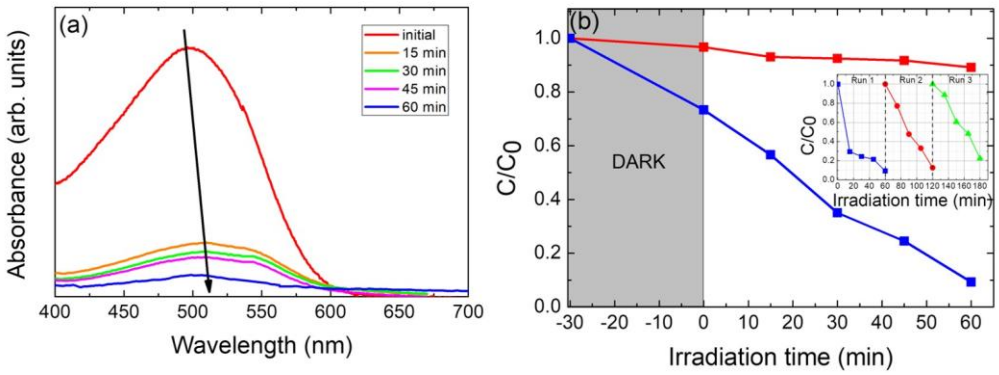

Figure 6. Photocatalytic degradation of Congo red azo dye in aqueous solution using nanoparticulate Cu_2ZnSnS_4 photocatalyst under AM1.5G simulated sunlight (100 mW cm^{-2}) illumination. (**a**) Absorbance spectra as a function of illumination time, demonstrating the photodegradation of Congo red dye against CZTS (see direction black arrow). (**b**) Relative concentration (C/C_0) versus time for photodegradation of Congo red azo dye in the presence (square blue symbols) and in the absence (square red symbols) of nanoparticulate Cu_2ZnSnS_4 photocatalyst, under AM1.5G, simulated sunlight (100 mW cm^{-2}) illumination. Inset: recyclability of nanoparticulate Cu_2ZnSnS_4 sample as photocatalyst for the photodegradation of Congo red azo dye.

The optimal photocatalyst portrays the best performance, and its photocatalytic property remains after several photodegradation cycles; in fact, the stable recyclability of one photocatalyst is vital for future practical applications [18,62]. Then, recycling photodegradation experiments of nanoparticulate Cu_2ZnSnS_4 photocatalyst have been carried out, as shown in the inset of Figure 6b. The measurement was repeated three times to evaluate the stability and reusability of the photocatalyst (see the Experimental section for details). The inset of Figure 6b gives the degradation rate for the 3 cycles. The photocatalytic performance remained stable after the third cycle (a minor deviation (~14%) from the initial degradation efficiency has been observed), which further confirms that the stability and reusability of nanoparticulate Cu_2ZnSnS_4 photocatalyst are reasonable. However, this decrease in the dye photo-degradation efficiency after several runs can be mainly due to the CZTS photocatalyst mass loss during the successive filtering and washing processes in between each photodegradation run cycle (processes carried out in order to remove and reuse the photocatalyst material).

4. Conclusions

The hydrothermal method proved to be a simple, low-cost, low-pollution route through which it was possible to obtain CZTS nanoparticles. XRD, RAMAN, XPS, and EDS confirmed that the structure and composition of the synthesized nanoparticles correspond to those of pure Cu_2ZnSnS_4. The formation of spherical and rod-like nanocrystals with mean sizes of 7 nm and 50–60 nm, respectively, has been found by TEM analysis. The EDS results confirmed that the synthesized nanopowder exhibited a homogeneous elemental distribution in the whole CZTS sample. From UV-visible data, the bandgap of CZTS films has been determined to be 1.5 eV, which is optimal for photocatalytic applications. The CZTS phase proved to be an excellent photo-catalyst for CR where 90.2% degradation could be achieved in just 60 min under solar simulation light irradiation, better than other photo-catalysts such as TiO_2, widely recognized for its good efficiency. The reusability experiment confirms the stability of the photocatalytic activity of the as-prepared CZTS nanopowder after three runs of the photodegradation process.

Author Contributions: Conceptualization, R.H., E.A.D. and P.S.N.; methodology, R.H., E.A.D. and P.S.N.; investigation, R.H., E.A.D., P.G.M., E.M.C., P.L.B., E.N.-A., E.A.D. and P.S.N.; resources, R.H. and E.A.D.; data curation, P.G.M., E.M.C., P.L.B., E.N.-A., E.A.D. and P.S.N.; writing—original draft preparation, R.H., E.A.D. and P.S.N.; writing—review and editing, R.H., E.A.D. and P.S.N.;

supervision, R.H. and E.A.D.; funding acquisition, R.H., E.N.-A. and E.A.D. All authors have read and agreed to the published version of the manuscript.

Funding: This work was partially supported by CSIC (Comisión Sectorial de InvestigaciónCientífica) of the Universidad de la República, Montevideo, Uruguay, and PEDECIBA—Física, Uruguay. This work was also partially supported by MICINN of Spain through the research project PID2020-117832RB-100. Finally, this work also received support from Consolidated DI project nº 039.314/2022, PUCV, Chile.

Data Availability Statement: Not applicable.

Acknowledgments: This work was partially supported by CSIC (Comisión Sectorial de InvestigaciónCientífica) of the Universidad de la República, Montevideo, Uruguay, and PEDECIBA—Física, Uruguay. The authors are grateful to MICINN of Spain through the research project PID2020-117832RB-100. The authors are also grateful for the support received from Consolidated DI project nº 039.314/2022, PUCV, Chile.

Conflicts of Interest: The authors declare no conflict of interest.

References

1. He, M.; Yan, C.; Li, J.; Suryawanshi, M.P.; Kim, J.; Green, M.A.; Hao, X. Kesterite Solar Cells: Insights into Current Strategies and Challenges. *Adv. Sci.* **2021**, *8*, 2004313. [CrossRef] [PubMed]
2. Wang, A.; He, M.; Green, M.A.; Sun, K.; Hao, X. A Critical Review on the Progress of Kesterite Solar Cells: Current Strategies and Insights. *Adv. Energy Mater.* **2023**, *13*, 2203046. [CrossRef]
3. Zhao, Y.; Yu, Z.; Hu, J.; Zheng, Z.; Ma, H.; Sun, K.; Hao, X.; Liang, G.; Fan, P.; Zhang, X.; et al. Over 12% efficient kesterite solar cell via back interface engineering. *J. Energy Chem.* **2022**, *75*, 321–329. [CrossRef]
4. Zaki, M.Y.; Sava, F.; Simandan, I.-D.; Buruiana, A.T.; Stavarache, I.; Bocirnea, A.E.; Mihai, C.; Velea, A.; Galca, A.-C. A Two-Step Magnetron Sputtering Approach for the Synthesis of Cu_2ZnSnS_4 Films from Cu_2SnS_3\ZnS Stacks. *ACS Omega* **2022**, *7*, 23800–23814. [CrossRef]
5. Altaf, C.T.; Abdullayeva, N.; Sankir, N.D.; Sankir, N.D. Copper-Based Chalcopyrite and Kesterite Materials for Solar Hydrogen Generation. In *Photoelectrochemical Solar Cells*; John Wiley & Sons, Ltd.: Hoboken, NJ, USA, 2018; pp. 251–303, ISBN 9781119460008.
6. Valdés, M.; Hernández, A.; Sánchez, Y.; Fonoll, R.; Placidi, M.; Izquierdo, V.; Cabas-Vidani, A.; Valentini, M.; Mittiga, A.; Pistor, P.; et al. A new approach for alkali incorporation in Cu2ZnSnS4 solar cells. *J. Phys. Energy* **2022**, *4*, 44008. [CrossRef]
7. Todorov, T.; Hillhouse, H.W.; Aazou, S.; Sekkat, Z.; Vigil-Galán, O.; Deshmukh, S.D.; Agrawal, R.; Bourdais, S.; Valdés, M.; Arnou, P.; et al. Solution-based synthesis of kesterite thin film semiconductors. *J. Phys. Energy* **2020**, *2*, 12003. [CrossRef]
8. Mamta; Maurya, K.K.; Singh, V.N. Comparison of Various Thin-Film-Based Absorber Materials: A Viable Approach for Next-Generation Solar Cells. *Coatings* **2022**, *12*, 405. [CrossRef]
9. Al Zoubi, T.; Al-Gharram, M.; Moustafa, M. Insights into the impact of defect states and temperature on the performance of kesterite-based thin-film solar cells. *Optik* **2022**, *264*, 169442. [CrossRef]
10. Nazligul, A.S.; Wang, M.; Choy, K.L. Recent Development in Earth-Abundant Kesterite Materials and Their Applications. *Sustainability* **2020**, *12*, 5138. [CrossRef]
11. Oueslati, S.; Pilvet, M.; Grossberg, M.; Kauk-Kuusik, M.; Krustok, J.; Meissner, D. Kesterite monograins for solar cells and water splitting applications. *Thin Solid Films* **2021**, *739*, 138981. [CrossRef]
12. Apostolopoulou, A.; Mahajan, S.; Sharma, R.; Stathatos, E. Novel development of nanocrystalline kesterite Cu2ZnSnS4 thin film with high photocatalytic activity under visible light illumination. *J. Phys. Chem. Solids* **2018**, *112*, 37–42. [CrossRef]
13. Zaman, M.B.; Mir, R.A.; Poolla, R. Growth and properties of solvothermally derived highly crystalline Cu2ZnSnS4 nanoparticles for photocatalytic and electrocatalytic applications. *Int. J. Hydrogen Energy* **2019**, *44*, 23023–23033. [CrossRef]
14. Alirezazadeh, F.; Sheibani, S. Facile mechano-chemical synthesis and enhanced photocatalytic performance of Cu2ZnSnS4 nanopowder. *Ceram. Int.* **2020**, *46*, 26715–26723. [CrossRef]
15. Hunge, Y.M.; Yadav, A.A.; Liu, S.; Mathe, V.L. Sonochemical synthesis of CZTS photocatalyst for photocatalytic degradation of phthalic acid. *Ultrason. Sonochem.* **2019**, *56*, 284–289. [CrossRef]
16. Sun, K.; Zhao, X.; Zhang, Y.; Wu, D.; Zhou, X.; Xie, F.; Tang, Z.; Wang, X. Enhanced photocarrier separation in novel Z-scheme Cu2ZnSnS4/Cu2O heterojunction for excellent photocatalyst hydrogen generation. *Mater. Chem. Phys.* **2020**, *251*, 123172. [CrossRef]
17. Semalti, P.; Sharma, V.; Sharma, S.N. A novel method of water remediation of organic pollutants and industrial wastes by solution-route processed CZTS nanocrystals. *J. Mater.* **2021**, *7*, 904–919. [CrossRef]
18. Raza, A.; Shen, H.; Haidry, A.A.; Shahzad, M.K.; Liu, R.; Cui, S. In-situ synthesis of mesoporous TiO2-Cu2ZnSnS4 heterostructured nanocomposite for enhanced photocatalytic degradation. *Appl. Surf. Sci.* **2020**, *505*, 144540. [CrossRef]
19. Xi, Z.-H.; Zhao, Y. Fabrication of Ti3+/TNS-CZTS heterostructures nanosheet arrays for photocatalytic enhancement. *Vacuum* **2022**, *201*, 111117. [CrossRef]

20. Mudike, R.; Sabbanahalli, C.; Sriramoju, J.B.; Bheemaraju, A.; Halligudra, G.; Muniyappa, M.; Narayanaswamy, M.P.; Kumar, C.A.; Shivaramu, P.D.; Rangappa, D. Copper zinc tin sulfide and multi-walled carbon nanotubes nanocomposite for visible-light-driven photocatalytic applications. *Mater. Res. Bull.* **2022**, *146*, 111606. [CrossRef]
21. Jain, S.; Singh, A.; Gupta, G.; Vijayan, N.; Sharma, S.N. Precursor ratio optimizations for the synthesis of colloidal CZTS nanoparticles for photocatalytic degradation of malachite green. *J. Phys. Chem. Solids* **2018**, *122*, 8–18. [CrossRef]
22. Mary, C.I.; Senthilkumar, M.; Manobalaji, G.; Prasanna, M.S.; Babu, S.M. Effect of different nanostructures of Cu2ZnSnS4 on visible light-driven photocatalytic degradation of organic pollutants. *J. Mater. Sci. Mater. Electron.* **2022**, *33*, 894–906. [CrossRef]
23. Hou, Z.; Li, Y.; Liu, J.; Shen, H.; Huo, X. The visible light-driven highly efficient photocatalytic properties of Cu2ZnSnS4 nanoparticles synthesized by a hydrothermal method. *New J. Chem.* **2021**, *45*, 1743–1752. [CrossRef]
24. Tiong, V.T.; Bell, J.; Wang, H. One-step synthesis of high quality kesterite Cu2ZnSnS4 nanocrystals—A hydrothermal approach. *Beilstein J. Nanotechnol.* **2014**, *5*, 438–446. [CrossRef]
25. Patro, B.; Vijaylakshmi, S.; Reddy, R.K.; Sharma, P. Microwave-assisted solvothermal synthesis of Cu2ZnSnS4 (CZTS) nanocrystals for photovoltaic applications. *Mater. Today Proc.* **2016**, *3*, 2786–2794. [CrossRef]
26. Gong, Z.; Han, Q.; Li, J.; Hou, L.; Bukhtiar, A.; Yang, S.; Zou, B. A solvothermal route to synthesize kesterite Cu2ZnSnS4 nanocrystals for solution-processed solar cells. *J. Alloys Compd.* **2016**, *663*, 617–623. [CrossRef]
27. Merrad, S.; Abbas, M.; Brahimi, R.; Trari, M. Study of Congo Red removal from aqueous solution by using the deficient perovskite SrTiO3-δ under solar light. *J. Mol. Struct.* **2022**, *1265*, 133349. [CrossRef]
28. Zhou, Y.; Ge, L.; Fan, N.; Xia, M. Adsorption of Congo red from aqueous solution onto shrimp shell powder. *Adsorpt. Sci. Technol.* **2018**, *36*, 1310–1330. [CrossRef]
29. Yahya, N.; Aziz, F.; Jamaludin, N.; Mutalib, M.A.; Ismail, A.; Salleh, W.W.; Jaafar, J.; Yusof, N.; Ludin, N.A. A review of integrated photocatalyst adsorbents for wastewater treatment. *J. Environ. Chem. Eng.* **2018**, *6*, 7411–7425. [CrossRef]
30. Khan, A.; Shah, S.J.; Mehmood, K.; Awais; Ali, N.; Khan, H. Synthesis of potent chitosan beads a suitable alternative for textile dye reduction in sunlight. *J. Mater. Sci. Mater. Electron.* **2019**, *30*, 406–414. [CrossRef]
31. Maksoud, M.I.A.A.; Fahim, R.A.; Bedir, A.G.; Osman, A.I.; Abouelela, M.M.; El-Sayyad, G.S.; Elkodous, M.A.; Mahmoud, A.S.; Rabee, M.M.; Al-Muhtaseb, A.H.; et al. Engineered magnetic oxides nanoparticles as efficient sorbents for wastewater remediation: A review. *Environ. Chem. Lett.* **2022**, *20*, 519–562. [CrossRef]
32. Maksoud, M.I.A.A.; El-Sayyad, G.S.; El-Khawaga, A.M.; Elkodous, M.A.; Abokhadra, A.; Elsayed, M.A.; Gobara, M.; Soliman, L.I.; El-Bahnasawy, H.H.; Ashour, A.H. Nanostructured Mg substituted Mn-Zn ferrites: A magnetic recyclable catalyst for outstanding photocatalytic and antimicrobial potentials. *J. Hazard. Mater.* **2020**, *399*, 123000. [CrossRef] [PubMed]
33. Elkodous, M.A.; El-Khawaga, A.M.; Abouelela, M.M.; Maksoud, M.I.A.A. Cocatalyst loaded Al-SrTiO3 cubes for Congo red dye photo-degradation under wide range of light. *Sci. Rep.* **2023**, *13*, 6331. [CrossRef] [PubMed]
34. Riha, S.C.; Parkinson, B.A.; Prieto, A.L. Solution-Based Synthesis and Characterization of Cu2ZnSnS4 Nanocrystals. *J. Am. Chem. Soc.* **2009**, *131*, 12054–12055. [CrossRef] [PubMed]
35. Cullity, B.D. *Elements of X-ray Diffraction*, 2nd ed.; Addison-Wesley Publishing Company Inc.: Reading, MA, USA, 1978; Volume 100–105, pp. 277–279.
36. Henríquez, R.; Vásquez, C.; Muñoz, E.; Grez, P.; Martín, F.; Ramos-Barrado, J.R.; Dalchiele, E.A. Phase-pure iron pyrite (FeS2) micro- and nano-sized crystals synthesized by simple one-step microwave-assisted hydrothermal method. *Phys. E Low-Dimens. Syst. Nanostruct.* **2020**, *118*, 113881. [CrossRef]
37. Li, Z.-S.; Wang, S.-R.; Jiang, Z.; Yang, M.; Lu, Y.-L.; Liu, S.-J.; Zhao, Q.-C.; Hao, R.-T. Cu2ZnSnS4 solar cells prepared by sulfurization of sputtered ZnS/Sn/CuS precursors. *Phys. B Condens. Matter* **2016**, *502*, 56–60. [CrossRef]
38. Su, Z.; Sun, K.; Han, Z.; Cui, H.; Liu, F.; Lai, Y.; Li, J.; Hao, X.; Liu, Y.; Green, M.A. Fabrication of Cu2ZnSnS4 solar cells with 5.1% efficiency via thermal decomposition and reaction using a non-toxic sol–gel route. *J. Mater. Chem. A* **2014**, *2*, 500–509. [CrossRef]
39. Ziti, A.; Hartiti, B.; Labrim, H.; Fadili, S.; Batan, A.; Tahri, M.; Ridah, A.; Mounkachi, O.; Benyoussef, A.; Thevenin, P. Characteristics of kesterite CZTS thin films deposited by dip-coating technique for solar cells applications. *J. Mater. Sci. Mater. Electron.* **2019**, *30*, 13134–13143. [CrossRef]
40. Fernandes, P.A.; Salomé, P.M.P.; da Cunha, A.F. Study of polycrystalline Cu2ZnSnS4 films by Raman scattering. *J. Alloys Compd.* **2011**, *509*, 7600–7606. [CrossRef]
41. Deepa, K.G.; Ramamurthy, P.C.; Singha, M.K. Mesoporous Cu2ZnSnS4 nanoparticle film as a flexible and reusable visible light photocatalyst. *Opt. Mater.* **2019**, *98*, 109492. [CrossRef]
42. Vishwakarma, M.; Thota, N.; Karakulina, O.; Hadermann, J.; Mehta, B.R. Role of graphene inter layer on the formation of the MoS2-CZTS interface during growth. *AIP Conf. Proc.* **2018**, *1953*, 100064. [CrossRef]
43. Schorr, S.; Gurieva, G.; Guc, M.; Dimitrievska, M.; Pérez-Rodríguez, A.; Izquierdo-Roca, V.; Schnohr, C.S.; Kim, J.; Jo, W.; Merino, J.M. Point defects, compositional fluctuations, and secondary phases in non-stoichiometric kesterites. *J. Phys. Energy* **2020**, *2*, 12002. [CrossRef]
44. Chaudhari, J.J.; Joshi, U.S. Fabrication of high-quality kesterite Cu2ZnSnS4 thin films deposited by an optimized sol–gel sulphurization technique for solar cells. *J. Mater. Sci. Mater. Electron.* **2020**, *31*, 14411–14420. [CrossRef]
45. NIST XPS Database. Available online: https://srdata.nist.gov/xps/main_search_menu.aspx (accessed on 10 November 2022).
46. Moulder, J.F.; Stickle, W.F.; Sobol, W.M.; Bomben, K.D. *Handbook of X-ray Photoelectron Spectroscopy*; Perkin-Elmer Corporation, Physical Electronics Division: Eden Prairie, MN, USA, 1992.

47. Zhang, X.; Guo, G.; Ji, C.; Huang, K.; Zha, C.; Wang, Y.; Shen, L.; Gupta, A.; Bao, N. Efficient Thermolysis Route to Monodisperse Cu2ZnSnS4 Nanocrystals with Controlled Shape and Structure. *Sci. Rep.* **2014**, *4*, 5086. [CrossRef] [PubMed]
48. Pankove, J.I.; Kiewit, D.A. Optical Processes in Semiconductors. *J. Electrochem. Soc.* **1972**, *119*, 156Ca. [CrossRef]
49. Kumarage, W.G.C.; Wijesundera, R.P.; Seneviratne, V.A.; Jayalath, C.P.; Dassanayake, B.S. Tunable optoelectronic properties of CBD-CdS thin films via bath temperature alterations. *J. Phys. D. Appl. Phys.* **2016**, *49*, 95109. [CrossRef]
50. Kisch, H. Chapter 4: Photoelectrochemistry. In *Semiconductor Photocatalysis: Principles and Applications*; Wiley-VCH: Weinheim, Germany, 2015; p. 59, ISBN 978-3-527-33553-4.
51. Mudike, R.; Bheemaraju, A.; Rasheed, T.; Singh, N.; Dhage, S.R.; Shivaramu, P.D.; Rangappa, D. Enhanced photocatalysis and photodetection using highly crystalline CZTS thin films optimized using stabilizers. *Ceram. Int.* **2022**, *48*, 35666–35675. [CrossRef]
52. Camara, S.M.; Wang, L.; Zhang, X. Easy hydrothermal preparation of Cu2ZnSnS4 (CZTS) nanoparticles for solar cell application. *Nanotechnology* **2013**, *24*, 495401. [CrossRef]
53. Hou, X.; Li, Y.; Yan, J.-J.; Wang, C.-W. Highly efficient photocatalysis of p-type Cu2ZnSnS4 under visible-light illumination. *Mater. Res. Bull.* **2014**, *60*, 628–633. [CrossRef]
54. Cho, J.W.; Ismail, A.; Park, S.J.; Kim, W.; Yoon, S.; Min, B.K. Synthesis of Cu2ZnSnS4 Thin Films by a Precursor Solution Paste for Thin Film Solar Cell Applications. *ACS Appl. Mater. Interfaces* **2013**, *5*, 4162–4165. [CrossRef]
55. Henríquez, R.; Grez, P.; Muñoz, E.; Dalchiele, E.A.; Marotti, R.E.; Gómez, H. Template-free non-aqueous electrochemical growth of CdO nanorods. *Thin Solid Films* **2011**, *520*, 41–46. [CrossRef]
56. Sivula, K. Mott–Schottky Analysis of Photoelectrodes: Sanity Checks Are Needed. *ACS Energy Lett.* **2021**, *6*, 2549–2551. [CrossRef]
57. Bard, A.J.; Faulkner, L.R. *Electrochemical Methods: Fundamentals and Applications*, 2nd ed.; John Wiley & Sons, Ltd.: Hoboken, NJ, USA, 2000.
58. Kisch, H. Chapter 5: Semiconductor Photocatalysis. In *Semiconductor Photocatalysis: Principles and Applications*; Wiley-VCH: Weinheim, Germany, 2015; p. 112, ISBN 978-3-527-33553-4.
59. Soleimani, F.; Salehi, M.; Gholizadeh, A. Comparison of visible light photocatalytic degradation of different pollutants by (Zn, Mg)xCu1-xBi2O4 nanoparticles. *Ceram. Int.* **2019**, *45*, 8926–8939. [CrossRef]
60. Putwa, S.; Curtis, I.S.; Dasog, M. Nanostructured silicon photocatalysts for solar-driven fuel production. *iScience* **2023**, *26*, 106317. [CrossRef] [PubMed]
61. Osterloh, F.E.; Parkinson, B.A. Recent developments in solar water-splitting photocatalysis. *MRS Bull.* **2011**, *36*, 17–22. [CrossRef]
62. Khan, J.; Tahir, K.; Wei, Y.; Albalawi, K.; Latif, S.; Abdulaziz, F.; El-Zahhar, A.A.; Saleh, E.A.M.; Al-Shehri, H.S.; Alghamdi, M.M. Preparation of Ca0.1Cu0.90Bi2O4 heterojunction with improved visible light photocatalytic performance of congo red: Kinetics and degradation mechanisms. *Inorg. Chem. Commun.* **2022**, *142*, 109607. [CrossRef]
63. Wang, L.; Li, J.; Wang, Z.; Zhao, L.; Jiang, Q. Low-temperature hydrothermal synthesis of α-Fe/Fe3O4 nanocomposite for fast Congo red removal. *Dalt. Trans.* **2013**, *42*, 2572–2579. [CrossRef]
64. Tian, J.; Tuo, B.; Wang, J.; Tang, Y.; Nie, G.; Yang, Y. Preparation of different crystal types TiO2 materials and its photodegradation performance in Congo Red wastewater. *Phase Transit.* **2022**, *95*, 707–725. [CrossRef]
65. Yang, G.; Yan, Z.; Xiao, T.; Yang, B. Low-temperature synthesis of alkalis doped TiO_2 photocatalysts and their photocatalytic performance for degradation of methyl orange. *J. Alloys Compd.* **2013**, *580*, 15–22. [CrossRef]
66. Shin, E.; Jin, S.; Kim, J.; Chang, S.-J.; Jun, B.-H.; Park, K.-W.; Hong, J. Preparation of K-doped TiO2 nanostructures by wet corrosion and their sunlight-driven photocatalytic performance. *Appl. Surf. Sci.* **2016**, *379*, 33–38. [CrossRef]
67. Guo, Y.; Wei, J.; Liu, Y.; Yang, T.; Xu, Z. Surfactant-Tuned Phase Structure and Morphologies of Cu2ZnSnS4 Hierarchical Microstructures and Their Visible-Light Photocatalytic Activities. *Nanoscale Res. Lett.* **2017**, *12*, 181. [CrossRef]
68. Ćurković, L.; Ljubas, D.; Juretić, H. Photocatalytic decolorization kinetics of diazo dye Congo Red aqueous solution by UV/TiO_2 nanoparticles. *React. Kinet. Mech. Catal.* **2010**, *99*, 201–208. [CrossRef]
69. Tekin, D. Photocatalytic Degradation Kinetics of Congo Red dye in a Sonophotoreactor with Nanotube TiO_2. *Prog. React. Kinet. Mech.* **2014**, *39*, 249–261. [CrossRef]
70. Vandarkuzhali, S.A.A.; Pugazhenthiran, N.; Mangalaraja, R.V.; Sathishkumar, P.; Viswanathan, B.; Anandan, S. Ultrasmall Plasmonic Nanoparticles Decorated Hierarchical Mesoporous TiO_2 as an Efficient Photocatalyst for Photocatalytic Degradation of Textile Dyes. *ACS Omega* **2018**, *3*, 9834–9845. [CrossRef] [PubMed]